

# The effect of dynamic temperatures on pebble dynamics and planet formation

Areli Castrejón<sup>1,2,3</sup>, Michiel Min<sup>2</sup>, Inga Kamp<sup>1</sup>, and Uffe Gråe Jørgensen<sup>3</sup>

<sup>1</sup> Kapteyn Astronomical Institute, University of Groningen, Groningen, The Netherlands

<sup>2</sup> Netherlands Space Research Institute (SRON), Leiden, The Netherlands

<sup>3</sup> Centre for ExoLife Sciences, Niels Bohr Institute, University of Copenhagen, Copenhagen, Denmark

October 31, 2024

## ABSTRACT

*Context.* To date, more than 5000 exoplanets have been discovered. The large majority of these planets have a mass between 1 and 17  $M_{\oplus}$ , making them so-called super-Earths and mini-Neptunes. The exact formation process for this abundant planet population has not yet been fully constrained.

*Aims.* Recent studies on the formation of these planets make various assumptions with regard to the disk. The primary mass budget, held in pebbles, is either assumed to have a constant size or is parametrized as a flux. Simplifications of the temperature structure, in the form of a static power law, do not consider the temperature evolution and high magnitudes of heating in the inner part of the disk. In this study, we aim to investigate the effect these simplifications of temperature and pebble sizes have on the pebble densities and resulting planet populations.

*Methods.* To constrain the timescales needed to form super-Earths, we developed a model for exploring a large parameter space. We included the effect of two different temperature prescriptions on a viscously accreting and spreading disk. We formed a pebble reservoir utilizing a simplified conversion timescale with a time- and radially dependent Stokes number for the dust. We then tracked the temporal evolution of the surface densities of gas, dust, and pebbles. Pebbles were allowed to drift and be accreted onto a growing protoplanet. As a planet grows, it exerts a torque on the disk, carving out a gap and affecting the pebble drift, before halting the growth of the planet.

*Results.* We find that viscous heating has a significant effect on the resulting mass populations, with the static power law showing smaller planets within 10 AU. Inside the dust-sublimation line, usually within 0.5 AU, planet formation is reduced due to the loss of planet-forming material. Our model replicates observed planet masses between Earth and mini-Neptune sizes at all radial locations, with the most massive planets growing in the intermediate turbulence of  $\alpha = 10^{-3}$ .

*Conclusions.* We conclude that a self-consistent treatment of temperature, with the inclusion of a dust-sublimation line, is important and could explain the high occurrence of super-Earths at short orbital separations.

## 1. Introduction

To date, more than 5000 exoplanets have been discovered (Akeson et al. 2013; Petigura et al. 2013; Mulders et al. 2018). The large majority of these planets are in the intermediate-mass range, between 1 and 17  $M_{\oplus}$ , and are thus so-called super-Earths and mini-Neptunes (Schneider et al. 2011; Bean et al. 2021). Despite the abundance of these planets in our galactic neighborhood, their formation processes have not yet been fully constrained.

One theory for their formation is the core accretion scenario, whereby larger planetesimals serve as planetary embryos and accrete other planetesimals, thereby forming the core of giant planets (Pollack et al. 1996). However, the timescale for planetary growth via planetesimal accretion is often longer than the lifetime of a protoplanetary disk (Pollack et al. 1996; Lambrechts & Johansen 2012; Johansen & Lambrechts 2017; Ormel et al. 2017). One solution to this timescale problem is accretion from smaller materials that are readily available in the disk. These smaller materials can be efficiently accreted once a planetesimal is formed, through processes such as the streaming instability (Johansen et al. 2015; Li & Youdin 2021). The formation of larger particles begins with collisions of interstellar size dust, resulting in coagulation (Brauer et al. 2008; Zsom et al. 2010; Birnstiel et al. 2012). However, particles do not just keep growing incessantly; there are various disturbances that play a

role in the formation of planetesimals. Planetesimal formation is tempered by fragmentation, bouncing, and radial-drift barriers (Brauer et al. 2008; Birnstiel et al. 2012). This hindrance in the formation of planetesimals results in an abundance of millimeter- to centimeter-sized particles. These larger particles, called pebbles, become an important part of the planet formation process. Reservoirs of material in the outer disk constantly replace the material being lost to planetary accretion and accretion onto the star (Weidenschilling 1977). The shorter timescale of accretion for pebbles allows planets to grow quickly, before the dissipation of the dusty and gaseous disk (Lambrechts & Johansen 2014; Bitsch et al. 2018; Lambrechts et al. 2019). As pebbles grow, they experience a headwind drag from the gaseous disk, which causes them to lose angular momentum and drift inward. The constant flux of pebbles paired with a large embryo-accretion cross section allows for efficient accretion onto a protoplanet (Whipple 1972; Ormel 2017). The growth from dust grains to pebbles and the subsequent planet formation processes are discussed in depth in the reviews by Liu & Ji (2020) and Drazkowska et al. (2023).

Various studies on pebble accretion show that super-Earths form easily within the lifetimes of protoplanetary disks (Bitsch et al. 2019b; Liu et al. 2019; Venturini et al. 2020; Savvidou & Bitsch 2023). Recent works on super-Earth formation show that the resulting mass for super-Earth planets is dependent on the pebble flux through the inner disk (Bitsch et al. 2019a; Liu

et al. 2019). Other works find that the pebble isolation mass, which is highly dependent on the temperature structure, has a significant effect on the final mass of the planet formed (Bitsch 2019; Savvidou & Bitsch 2021). Recently, Venturini et al. (2020) found that the largest planets formed within the water ice line are at most 5 Earth masses.

In this work, we aim to investigate the effects that viscous heating with dust sublimation, self-consistent pebble sizes, and 1D gap formation have on the formation of super-Earth populations. Our main motivation for this study was to better understand pebble drift, which is set by the headwind velocity, a quantity that is dependent on the disk temperature. A power law for the temperature is commonly used, representing a disk heated only by the central star (Ida et al. 2016). However, temperatures in the inner 5 AU of the disk can reach higher levels due to viscous heating (Min et al. 2011; Bitsch et al. 2015; Ida et al. 2016). At high temperatures, dust can sublimate, depending on its composition. As the dust sublimates (Kobayashi et al. 2011), it removes opacity from the disk, causing the temperature to drop and remain constant, independent of radius, leading to a so-called dust thermostat (Min et al. 2011). These changes in temperature structure should likely affect the radial evolution of pebble densities.

In this work, we focused on the growth of planets via pebble accretion onto a preformed protoplanetary embryo. We followed the growth of the planet and its corresponding gap carving in the gaseous disk (Lin & Papaloizou 1986; Alibert et al. 2005). Earlier 1D studies did not investigate how a gradual gap-formation process affects the pebble flux and thus planet buildup. Here, we investigated how this process compares to works that used the pebble isolation mass to halt planet growth. We followed the temperature evolution of the disk using two different temperature prescriptions: (i) a model that includes a viscous and passively heated disk with a dust thermostat and dust removal and (ii) a passively heated power-law model. We investigated the effect that different temperature prescriptions have on pebble evolution and subsequently on the formation of planets. Based on our findings, we performed a parameter study, varying the viscosity, embryo location, and insertion time.

This paper is structured as follows. In Sect. 2, we explain our semi-analytic model in detail. This includes the different temperature prescriptions, the formation of pebbles from dust while including growth limits, how a planet carves a gap in the disk, and the initial timeline for planet formation. In Sect. 3, we present the results from our temperature prescriptions on pebble growth and transfer. We then interpret the implications for planet formation and pebble formation in Sect. 4. Finally, we summarize our findings in Sect. 5.

## 2. Methods

Exploring the parameter space for planet formation requires a swift model with moderate complexity. As such, we developed a computationally fast model for the temporal evolution of gas, dust, and pebble densities, while intending to capture most aspects of the evolution in a realistic manner. We used a simplified recipe to describe how dust is turned into pebbles as a function of time and radius. We inserted Moon-mass protoplanets into the disk and let them grow through pebble accretion. Once a planet grows large enough, it can carve a gap in the disk, leading to a pressure bump and the slowdown of pebble accretion. We ran a suite of models, exploring two different assumptions for disk temperatures. Within each temperature prescription, the variable

quantities were the disk viscosity and the initial time of embryo insertion.

### 2.1. Protoplanetary disk model

We began with the equations of conservation of mass and angular momentum for a gaseous disk (Lynden-Bell & Pringle 1974),

$$\frac{\partial \Sigma_g}{\partial t} = \frac{1}{r} \frac{\partial}{\partial r} \left[ \Sigma_g r (u_g + u_\tau) \right], \quad (1)$$

where the gas velocity,  $u_g$ , is given by

$$u_g = \frac{-3}{\Sigma_g \sqrt{r}} \frac{\partial}{\partial r} (\Sigma_g \nu r), \quad (2)$$

and  $u_\tau$  is a velocity term arising from torques once a planet is large enough to disturb the disk. This term,  $u_\tau$ , is further discussed in Sect. 2.6. Here,  $\Sigma_g$  is the gaseous surface density and  $r$  is the radial location in the disk. The viscosity in the disk,  $\nu$ , is given by

$$\nu = \alpha c_s H, \quad (3)$$

where  $\alpha$  is a dimensionless parameter that describes the turbulent strength (Shakura & Sunyaev 1973). The sound speed,  $c_s$ , and scale height,  $H$ , are given by

$$c_s = \sqrt{\frac{k_B T}{\mu m_p}} \quad (4)$$

and

$$H = \frac{c_s}{\Omega}, \quad (5)$$

where  $k_B$  is the Boltzmann constant,  $T$  is the midplane temperature in the disk,  $\mu$  is the mean molecular weight of the gas (assumed to be molecular), and  $m_p$  is the proton mass. The Keplerian frequency,  $\Omega$ , is given by

$$\Omega = \sqrt{\frac{GM_*}{r^3}}, \quad (6)$$

with  $G$  and  $M_*$  as the gravitational constant and mass of the star, respectively. We set our initial gas surface density as a function of radial distance,  $r$ , to a tapering power law, namely the one used in Lynden-Bell & Pringle (1974),

$$\Sigma_{g,0} = (2 - \gamma) \frac{M_{\text{disk}}}{2\pi r_c^2} \left( \frac{r}{r_c} \right)^{-\gamma} \exp\left(-\frac{r}{r_c}\right), \quad (7)$$

where  $M_{\text{disk}}$  is the disk mass,  $r_c$  is the characteristic radius, and  $\gamma$  is the power-law exponent. The initial dust surface density was set to

$$\Sigma_{d,0} = Z_0 \cdot \Sigma_{g,0}, \quad (8)$$

where  $Z_0$  is the initial dust-to-gas ratio.

## 2.2. Temperature structure

We set out to investigate the effect that different temperature structures have on the evolution of a protoplanetary disk and, by association, on the planet formation process. Previous studies on planet formation have treated the temperature structure as being dominated by only stellar irradiation (Armitage 2010). To investigate the effect of this assumption, we investigated two different temperature structures. We considered heating from stellar irradiation and viscous stresses, following the analytical temperature model in Min et al. (2011). The temperature is dominated by viscous heating in the inner disk and by stellar irradiation in the outer disk. Upon determining the initial gas surface density, we calculated the temperature in the midplane of the disk. The equation for the viscous temperature is

$$T_{\text{vis}} = \left[ \frac{27}{128} \left( \frac{\Sigma_{\text{g}} \kappa_{\text{R}} \alpha k_{\text{B}} Z \Omega}{\sigma \mu m_{\text{p}}} \right) \right]^{1/3}, \quad (9)$$

where  $\kappa_{\text{R}}$  is the Rosseland mean opacity, and  $Z$  is the local dust-to-gas ratio. This dust-to-gas ratio changes over time and differs from our initial dust-to-gas ratio,  $Z_0$ . The temperature from irradiation is

$$T_{\text{irr}} = \left[ \varphi \frac{L_{\star}}{4\pi\sigma r^2} \right]^{1/4}, \quad (10)$$

where  $\varphi$  is the grazing angle, and  $L_{\star}$  is the stellar luminosity. We added the contributions from the viscous and irradiative energies to find our final midplane temperature,

$$T^4 = T_{\text{irr}}^4 + T_{\text{vis}}^4. \quad (11)$$

### 2.2.1. Standard model

As reported by Min et al. (2011), the temperature in the inner disk reaches high enough temperatures to exceed the silicate sublimation temperature. The balance between the deposition and sublimation of matter causes a thermostat effect, limiting the midplane temperature to the silicate sublimation threshold. When temperatures reach a value higher than the silicate sublimation temperature given by Eq. (9), dust sublimation will lower the temperature until a balance is reached at  $\approx 1500$  K (Kobayashi et al. 2011). This sublimation process reduces the available material for planet formation and results in a flat temperature structure in the inner parts of the disk. To reproduce this flat temperature in the inner disk, we calculated the  $Z$  needed for  $T=1500$  K and then removed the dust and added it to our gas component. We refer to this reduced dust and temperature model as our standard model.

### 2.2.2. Power-law model

To be able to compare our results to previous works, we also used a static power-law temperature of

$$T_{\text{const}} = 186 \left( \frac{r}{\text{AU}} \right)^{-1/2} \text{ K}. \quad (12)$$

We chose this temperature structure to coincide with the temperature profile in the outer disk regions of our previous models, as seen in Fig. 1. This equation is also a solution for Eq. (10) using our model parameters. We assume that this temperature structure does not evolve in time and refer to this simplified temperature prescription as our power-law model.

## 2.3. Growing from dust to pebbles

In a disk, not all dust particles are identical. Particles of different sizes behave differently based on their Stokes number, a quantity that defines the particles' coupling to the gas (see, e.g., Ormel 2017). The Stokes number in the Epstein drag regime (Brauer et al. 2008) is given by

$$\text{St} = \frac{\pi a \rho_{\text{s}}}{2 \Sigma_{\text{g}}}, \quad (13)$$

where  $\rho_{\text{s}}$  is the material density of the grain, and  $a$  is the size of the grain. Ormel (2017) defines pebbles as falling within the range  $10^{-2} \leq \text{St} < 1$ . Therefore, pebbles can range in physical size from millimeter- to centimeter-sized particles (Pérez et al. 2015).

Pebbles are a vital component in planet formation since they experience a gas drag that slows down their motions, allowing for faster protoplanetary embryo growth (Ormel 2017). We followed previous works that used a simplified approach to calculate the maximum sizes of grains (Birnstiel et al. 2012; Drażkowska & Alibert 2017; Venturini et al. 2020). This simplified approach determines the available pebble population as a function of time and radius. We subdivided our disk solids into two distinct populations, small grains coupled to the gaseous disk motions (dust) and larger grains that can drift through the disk (pebbles). We began with the equation to grow to a determined size from Brauer et al. (2008),

$$a = a_0 \exp \left( \frac{\Omega \Sigma_{\text{d}} t}{\Sigma_{\text{g}}} \right). \quad (14)$$

The equation states that the growth of a particle of size,  $a$ , is dependent on the initial particle size,  $a_0$ , and the exponent of the local dust-to-gas ratio, the Keplerian frequency, and the time elapsed. This assumption is valid for particles with a Stokes number less than unity.

However, the growth of grains does not continue in this way up to planetary sizes. Particle growth is subject to limiting factors, two of which are determined by turbulent fragmentation and radial drift. In the fragmentation case, dust grains can fragment into smaller particles due to the relative motions caused by turbulence in the disk. In this case, the maximum grain size is given by

$$a_{\text{frag}} = \frac{2 \Sigma_{\text{g}} v_{\text{frag}}^2}{3 \pi \rho_{\text{s}} \alpha c_{\text{s}}^2}, \quad (15)$$

where  $v_{\text{frag}}$  is a free parameter that can range from 100 to  $10^3$  [cm/s] (Gundlach & Blum 2015; Musiolik & Wurm 2019). The second limiting factor is the balance between the growth timescale and the drift timescale. This arises because the timescale for particle drift can be similar to or less than the time it takes to grow to a larger grain size. This particle size is given by

$$a_{\text{drift}} = \frac{2 \Sigma_{\text{d}} v_{\text{k}}^2}{\pi \rho_{\text{s}} c_{\text{s}}^2} \left| \frac{\partial \log P}{\partial \log r} \right|^{-1}. \quad (16)$$

Based on these three criteria, we chose the critical size of our pebbles to be

$$a_{\text{crit}} = \min \left\{ a_{\text{drift}}, a_{\text{frag}}, a_0 \exp \left( \frac{\Omega \Sigma_{\text{d}} t}{\Sigma_{\text{g}}} \right) \right\}. \quad (17)$$

Knowing the critical size, we arrived at an analytical solution for the critical time to transform dust into pebbles of a maximum

size using Eq. (14). Plugging our critical size,  $a_{\text{crit}}$ , into  $a$ , we were able to solve for  $t_{\text{crit}}$ :

$$t_{\text{crit}} = \log \left( \frac{a_{\text{crit}}}{a_0} \right) \frac{\Sigma_g}{\Omega \Sigma_d}. \quad (18)$$

Over time, we populated our pebble surface density through a source term dependent on the dust surface density,

$$S_p = \Sigma_d \cdot \left[ 1 - \exp \left( \frac{-t}{t_{\text{crit}}} \right) \right]. \quad (19)$$

This allowed for the growth transition from dust to pebbles to proceed smoothly. Theoretically, as the model progresses, the exponential reaches a value of unity, resulting in a total conversion of dust into pebbles.

In a protoplanetary disk, however, the efficiency of dust-to-pebble conversion will not be fully efficient since fragmentational collisions will erode pebbles, replenishing the small grains. We assumed that the fragmentation of pebbles results in grains that are 1 micron in size. Hence, we did not fully deplete our dust population and opted to keep a certain dust fraction. This simplification allows the viscous temperature in the disk to remain high, as the replenishment of small grains keeps the opacity high. We chose to limit our particle populations, keeping 75% as pebbles and 25% as dust, which we achieved by first calculating the ratio of pebbles making up the total solid mass using

$$\Sigma_{\text{tot}} = \frac{\Sigma_p}{\Sigma_p + \Sigma_d}. \quad (20)$$

If this quantity was larger than 75%, we removed the excess pebbles and added them back into the dust surface density. This ensured enough dust to simulate viscous heating and an evolving temperature structure in the inner disk.

#### 2.4. Pebble evolution

Pebbles orbiting a gaseous disk attempt to move on Keplerian orbits but experience an aerodynamic headwind due to gas moving at sub-Keplerian speed. Pebbles drift toward the inner disk according to the equation from Birnstiel et al. (2010, 2012),

$$\frac{\partial \Sigma_p}{\partial t} = -\frac{1}{r} \frac{\partial}{\partial r} \left[ r \left( \Sigma_p u_r - D_d \Sigma_p \frac{\partial}{\partial r} \left( \frac{\Sigma_p}{\Sigma_g} \right) \right) \right] + S_p, \quad (21)$$

where  $\Sigma_p$  is the pebble surface density, and  $D_d$  is the dust diffusion coefficient, usually given by this equation from Youdin & Lithwick (2007):

$$D_d = \frac{\nu}{1 + \text{St}^2}. \quad (22)$$

The radial velocity of the pebbles,  $u_r$ , contains two contributions. The first term is the drag term due to the gas velocity,  $u_g$ , which drags the pebbles to an extent, as they do not fully decouple from the gas. When a planet was introduced, we included the velocity due to the planetary torque,  $u_\tau$ . The second contribution is the radial drift velocity,  $u_n$ , with respect to the gas. Gas in a protoplanetary disk experiences the force of its own pressure support, which causes it to move in a sub-Keplerian fashion. This leads to moving pebbles experiencing a constant headwind, which causes them to lose angular momentum and drift inward.

Both of these velocities scale depending on the Stokes number of the particles, such that the total radial velocity is given by

$$u_r = \frac{1}{1 + \text{St}^2} (u_g + u_\tau) - \frac{\text{St}}{1 + \text{St}^2} 2u_n, \quad (23)$$

where the drift velocity,  $u_n$ , is given by

$$u_n = -\frac{c_s^2}{2\Omega r} \frac{\partial \log P}{\partial \log r}. \quad (24)$$

The midplane pressure,  $P$ , that determines the drift velocity is given in our model by

$$P = \rho_g c_s^2, \quad (25)$$

where the midplane gas density,  $\rho_g$ , is

$$\rho_g = \frac{\Sigma_g}{\sqrt{2\pi} H}. \quad (26)$$

#### 2.5. Planet formation

To model the planet formation process, we inserted a planetary embryo of  $M_{\text{pl},0} = 10^{-2} M_\oplus$  at different disk times and radial positions. We assumed the embryo is formed through other processes beyond the scope of this work. One possible mechanism for embryo formation is the streaming instability, in which high-density filaments of material collapse into planetary embryos (Youdin & Goodman 2005; Johansen et al. 2007, 2015). Here, we set aside planet migration and did not track the chemical composition of the building blocks. This will be investigated in future works.

A planet exerts a gravitational influence in the disk over a distance according to its Hill radius,

$$r_{\text{Hill}} = r_{\text{pl}} \left( \frac{M_{\text{pl}}}{M_*} \right)^{1/3}, \quad (27)$$

where  $r_{\text{pl}}$  and  $M_{\text{pl}}$  are the radial planet location and the planet mass, respectively. We opted to insert Moon-mass embryos into our disk, as they accrete pebbles more effectively. The prescription for the most efficient 2D pebble accretion is given by (Ormel 2017)

$$\dot{M}_p = 2r_{\text{Hill}}^2 \Omega \text{St}^{2/3} \Sigma_p. \quad (28)$$

#### 2.6. Planet-disk interactions

As the planet grows, it also begins to exert a tidal force on the disk. This torque can clear a gap in the gaseous disk, depending on the planet mass. We used the formulation in Lin & Papaloizou (1986), where the momentum exchange between the planet and the disk allows the planet to clear a gap in the gas surface density. This effect translates into a change in the gas velocity on both sides of the planet location. We call this velocity  $u_\tau$ , and it is given by

$$u_\tau = \frac{f_\Lambda \sqrt{GM_\odot r}}{r} \left( \frac{M_{\text{pl}}}{M_\odot} \right)^2 \left( \frac{r}{\max(|r - r_{\text{pl}}|, H)} \right)^4, \quad (29)$$

where  $f_\Lambda$  is a numerical constant. This velocity either accelerates or diminishes the flow of pebbles, depending on the location in the disk. Pebbles located between the planet and the star are accelerated toward the star, while pebbles beyond the planet are accelerated toward the outer disk. This reversal in the gas velocity

Table 1: Parameters used throughout this paper.

Disk Parameters		
Parameter	Explanation	Value
$\gamma$	power-law exponent	0.8
$r_c$	critical disk radius	60 AU
$M_{\text{disk}}$	disk mass	$0.1 M_{\odot}$
$\mu$	average molecular mass	2.4
$\varphi$	grazing angle	0.05
$L_*$	stellar luminosity	$1 L_{\odot}$
$M_*$	stellar mass	$1 M_{\odot}$
$Z_0$	initial dust-to-gas ratio	0.01
$\kappa_R$	Roseland mean opacity	508
$\alpha$	alpha viscosity	$[10^{-4} - 10^{-2}]$
Planet/Pebble Parameters		
$M_{\text{pl},0}$	planetary embryo mass	$10^{-2} M_{\oplus}$
$t_0$	initial time	$[5 \times 10^4 - 10^6]$ years
$\rho_s$	grain material density	$1.25 \text{ [g/cm}^3\text{]}$
$a_0$	initial dust size	$10^{-4} \text{ [cm]}$

leads to a halt in the pebble drift and the formation of a pressure bump outside of the planet location. This behavior prevents pebbles from entering the planet location, halting the planet formation process. Recent studies of planet formation used the pebble isolation mass to calculate the end of growth via pebble accretion (Lambrechts et al. 2014; Bitsch et al. 2018). We investigated how a gradual stop of the formation process affects the evolution of pebble dynamics and super-Earth formation in 1D models.

### 2.7. Modeling setup

We evolved our disk for 3 Myr using the finite-volume approach, which allowed us to use a complex and computationally fast model. The model's computation time was determined by the time step of the model. We limited the time step based on the three disk populations. We ensured that the gas, dust, and pebble densities did not change by more than 0.1% of their previous value. This results in the best stability for disk evolution and mass conservation.

### 2.8. Model parameters

We defined our disk quantities on two logarithmically spaced grids. The first comprised  $N_1 = 200$  points between  $r_{\text{in}} = 0.2$  AU and  $r_{\text{out}} = 1000$  AU. The second grid comprised  $N_2 = 200$  points 0.5 AU from the planet in both directions (toward and away from the star) to accurately capture the gap carving. The code then solves the disk structure, calculates the smallest time step from the previously described quantities, and advances the model in time. We began with a solar-mass star and a surrounding disk of  $0.1 M_{\odot}$ . We varied the viscosity in our disk from  $\alpha = [10^{-4} - 10^{-2}]$  on a logarithmically spaced grid of 7 points. We also investigated the effect that embryo formation times have on the final planet mass, using a logarithmically spaced grid of 20 points from  $t_0 = [5 \times 10^4 - 1 \times 10^6]$  years. Our initial disk parameters are shown in Table 1. We inserted the individual protoplanets at 0.25, 1, 2, 5, and 10 AU.

## 3. Results

We began by investigating the implications of our two different temperature models. We ran a set of six simulations that varied

our two temperature prescriptions and three different viscosities without inserting planetary embryos. We first compared the temporal evolution of the disk temperature for the two temperature prescriptions, and then quantified the effect on the pebble surface density. Lastly, we ran an array of planet formation models to visualize the effects of different pebble surface densities on growing planets. For this, we ran 140 models for 7 different viscosities and 20 embryo insertion times for each temperature prescription. We reran these simulations at radial locations of 0.25, 1, 2, 5, and 10 AU.

### 3.1. Differing temperature treatments

We first investigated the differences between temperature prescriptions and their evolution over the disk's lifetime. We began by varying the viscosity for each formulation. Figure 1 shows the evolving temperature structure for two prescriptions. Larger viscosities have a noticeable effect on the disk temperature in the inner disk. Initially, the value of  $T$  at 1 AU varies by a factor of five between viscosities of  $10^{-2}$  and  $10^{-4}$ . Higher temperatures also extend farther into the disk, with the higher alpha value deviating from the power-law case by up to 30 AU. After  $3 \times 10^6$  years, the temperature is reduced for all viscosities, and viscous heating only remains important within 1 AU of the star. This change in temperature can have implications for temperature-dependent quantities, such as pebble drift.

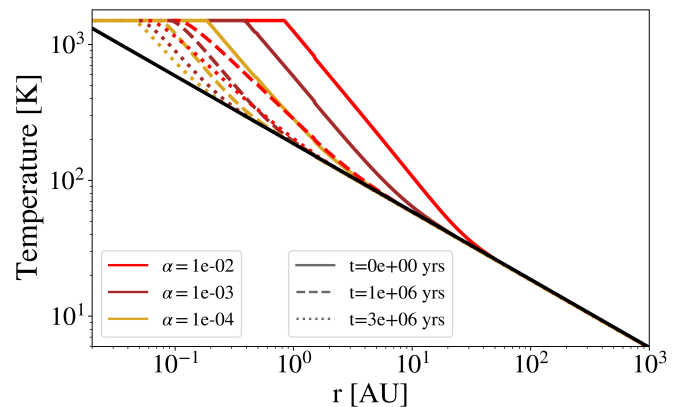


Fig. 1: Temperature structure of the disk as a function of distance from the central star. The solid red, brown, and orange lines correspond to the initial temperature profiles using viscosities of  $10^{-2}$ ,  $10^{-3}$ , and  $10^{-4}$ , respectively. The solid black line is a power-law temperature profile that remains static, chosen to match the outer disk temperature of a passively heated disk. The dashed and dotted lines show the evolution of the temperature at 0,  $10^6$ , and  $3 \times 10^6$  years.

### 3.2. Effect on pebble surface density

One of the evolving quantities affected by temperature is the pebble surface density. Figure 2 shows the evolution of pebbles as a function of radius up to  $10^6$  years in the absence of protoplanets. We chose to show the intermediate case of an alpha value equal to  $10^{-3}$ . At  $t = 1 \times 10^3$  years, the pebble surface densities for the standard and power-law cases are similar throughout the disk, except for the location of the dust sublimation front at 0.5 AU, where the standard case shows a reduced pebble surface density.

The reduction in this part of the disk is due to the removal of dust, which in turn is due to the thermostat effect at  $T = 1500$  K; this results in decreased formation of pebbles due to the lack of dust available. Initially, the power-law model shows an increased surface density at the inner edge of the disk, differing by three orders of magnitude from the standard model. As the disk evolves, the pebble surface density decreases in all cases, as inward drift removes pebbles through the inner boundary. At  $t = 5 \times 10^5$  years, the pebble surface density for the standard treatment and the power-law case show a reduction of pebbles in the outer disk and an enhancement of pebbles in the inner disk. We note that the surface densities at 1 AU differ, with the power law having a smaller enhancement than our standard case. By  $t = 10^6$  years, the outer pebble density has migrated inward, leading to a pebble-rich disk inside 10 AU. We note that the largest difference in the pebble surface densities occurs where dust sublimation becomes significant. Star-ward of this location, the difference in the pebble surface density is up to four orders of magnitude.

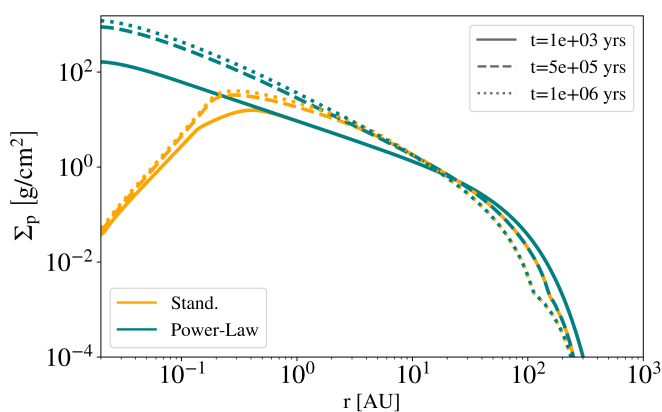


Fig. 2: Temporal evolution of the pebble surface density as a function of radius. The solid orange and teal lines correspond to the pebble surface density for our standard and power-law cases, respectively. The orange lines show the dust-sublimation front beginning at around 0.5 AU. The solid, dashed, and dotted-dashed lines correspond to disk times of  $10^3$  years,  $5 \times 10^5$  years, and 1 Myr, respectively.

### 3.3. Effect on planet formation

In the previous section, we explored the effect of the different temperature prescriptions on the evolution of the pebble surface density in the absence of planets. We found that with a non-evolving temperature structure, there was more pebble availability inside the dust-sublimation front. Since pebbles form the basis of planet growth in our model, we expected the effect on planet populations to be nonzero. We tested this by placing planetary embryos at 0.25, 1, 2, 5, and 10 AU. We varied the initial time at which the planetary embryo was inserted. The embryos then grew through pebble accretion until we stopped the disk evolution at 3 Myr.

Figure 3 shows the final masses for planets formed at 0.25 AU. The location of these planets is within the dust-sublimation front, where the availability of dust and pebbles was reduced. The noticeable difference between the models is that with the standard model, planets do not grow larger than 1 Earth mass at alpha values larger than  $10^{-3}$ , whereas the power-law model

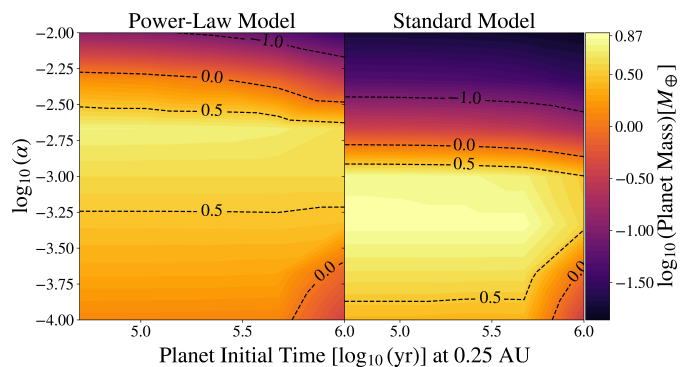


Fig. 3: Planet formation grid at 0.25 AU. We show the final planet masses after  $3 \times 10^6$  years of evolution as a function of alpha viscosity and the time a planetary embryo is inserted in the disk. Left panel: Power-law case with static irradiative heating. Right panel: Standard model with a dust-sublimation front that causes a temperature cap. The contours in black show the final planet masses differing by orders of 0.5 dex.

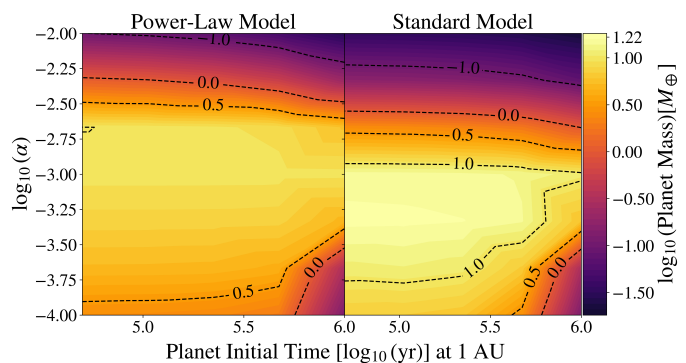


Fig. 4: Same as Fig. 3 but at 1 AU in the disk.

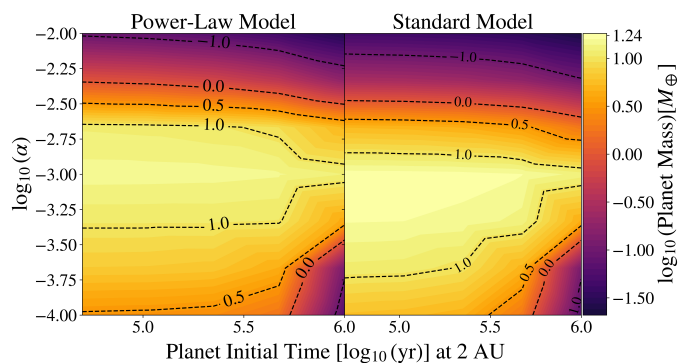


Fig. 5: Same as Fig. 4 but at 2 AU in the disk.

shows a distribution of planets with masses larger than that of Earth across all alpha values. At this location, the largest planets formed are 7 Earth masses for our standard case and 6 Earth masses for the power-law case. Both panels also show preferential growth for alpha values of  $10^{-3}$  in the power-law case, whereas the standard case shows a preference for alpha values below  $10^{-3}$ .



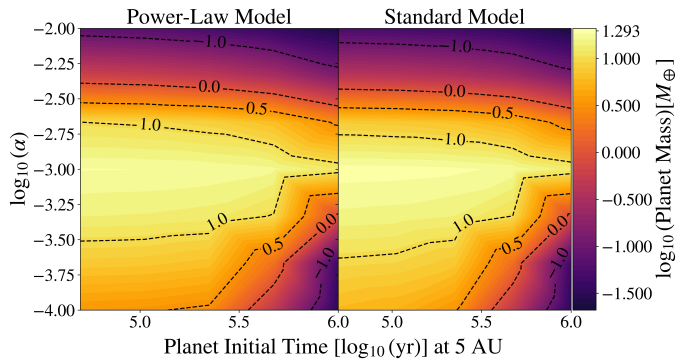


Fig. 6: Same as Fig. 4 but at 5 AU in the disk.

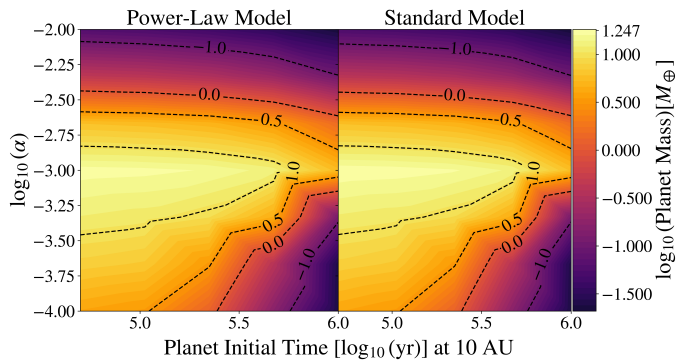


Fig. 7: Same as Fig. 4 but at 10 AU in the disk.

Figure 4 shows the final masses for the different planets formed at 1 AU. At this location, the standard model shows more massive planets than the power-law case. The most massive planet formed is 16 Earth masses. We find a correlation between earlier growth times and more massive planets, with the majority of planets lying between 1 and 16 Earth masses. High alpha values of  $\approx \alpha = 10^{-2}$  do not allow for the formation of planets larger than 1 Earth mass. This is due to the gaseous disk spreading for larger alphas, dragging pebbles along, and reducing the amount of planet-forming material in the disk. This is also coupled with the fact that higher alphas lead to lower particle sizes and Stokes numbers due to fragmentation. Particles with lower Stokes numbers lead to inefficient pebble accretion. The figure shows a preference for planet formation at intermediate alpha values. This is explained in detail in Sect. 4.1. The fixed power law shows a similar distribution of planet masses as a function of viscosity and embryo insertion time. However, they are generally 40-60 % lower in mass compared to the standard case. If the embryo is placed at 2 AU (Fig. 5), the largest planets formed for our standard temperature case are on the order of 17 Earth masses. This is a slight increase in mass from planets formed at 1 AU. In the power-law case, the largest planet is on the order of 15 Earth masses. However, we note that the power-law case can now form planets larger than 10 Earth masses at this orbital separation.

Next, we placed a planetary embryo at 5 AU (Fig. 6). The standard temperature model continues to show a varied distribution of planet masses larger than Earth, with the most massive being 20 Earth masses. The static power-law model shows a similar distribution of planets, with the largest being 18 Earth masses. Therefore, larger orbital separations result in a marginal

increase in planetary masses. This is to be expected, as the Hill radius for a Moon-mass embryo grows more the farther out it is placed in the disk.

Lastly, we placed a planetary embryo at 10 AU (Fig. 7). In all models, the largest planets are  $\approx 17$  Earth masses, falling within the mini-Neptune regime. The mass difference in the largest planets at this location is less than 0.5 Earth masses. At this orbital separation, we find that both cases are similar in their planet production.

Thus, we find that a self-consistent evolving temperature structure results in differences in the pebble surface evolution, which translates into a difference in the final planet mass. Dynamic temperatures at 1 AU lead to an increase of 60% in the final planet mass for the largest planet. However, as we move radially outward and the dominant temperature becomes the irradiation from the star, the mass increase diminishes to only 3% at 10 AU. When a planet is placed within the dust-sublimation line, the largest planets are of super-Earth sizes, and the power law shows a larger distribution of super-Earth planets. This is to be expected since the power-law prescription has a greater availability of pebbles for planet formation.

## 4. Discussion

### 4.1. The $\alpha$ "sweet spot"

At all radial locations in the disk, we find an optimal growth mode for planets when  $\alpha$  is equal to  $10^{-3}$ . This "sweet spot" can be explained by the gap carving in our disk. At one extreme, a low alpha leads to smaller planets carving a significant gap, stopping the flow of pebbles and stunting the planet's growth. At the other extreme, a high alpha impedes a planet from forming a significant gap, and material streams past the planet too quickly, without being accreted. This results in the reduced planet masses at the boundaries of our  $\alpha$  parameter exploration. The effect of an intermediate alpha is most noticeable when we compare the two different temperature structures (Fig. 8). In Sect. 3.2, we established that a passively heated disk results in an abundance of pebbles due to lack of sublimation. This enhances pebbles in the inner disk and allows a planet to grow large enough to form a gap by  $t = 7 \times 10^5$  years. The insert shows the gap formation for our two temperature prescriptions. The power-law temperature shows a noticeable gap at all times, while the standard case lacks any deviation, even at 1 Myr. After 2 Myr, the planet in the standard case has grown large enough and carves a significant gap in the pebble surface density. Therefore, a dynamic temperature prescription suppresses gap formation in a 1D context. This lack of a gap allows material to enter the planet's Hill radius, continuing the growth to higher masses than those at higher or lower alpha values. This behavior causes the "sweet spot" for planet growth at intermediate alpha values. Figure 9 shows that the power-law case grows to its final planet mass more quickly than the standard prescription. This early growth is due to a larger pebble reservoir (Fig. 2). This leads to gap carving at an earlier time, which stunts the growth of the planet.

### 4.2. Gas accretion

Our model produces planets within Earth to mini-Neptune masses. We did not model runaway gas accretion and allowed our planets to grow to masses of  $\approx 10 M_{\oplus}$  solely through the accretion of pebbles. In fact, it has been shown that planets already begin accreting a gaseous envelope in early stages (Ikoma et al. 2000). At 5 Earth masses, the accretion of a gaseous envelope

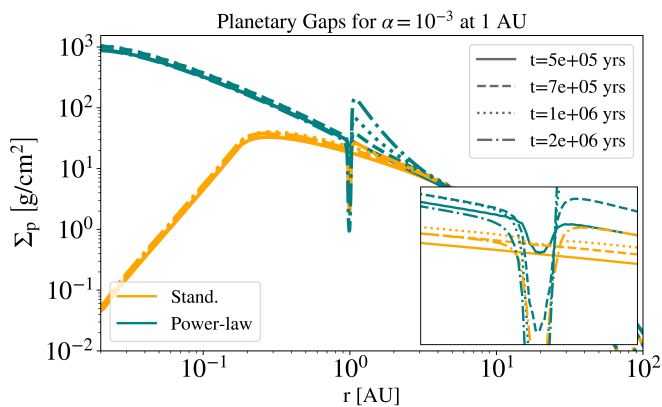


Fig. 8: Gap formation in the pebble surface density by planets in a disk at 1 AU with an alpha value of  $10^{-3}$  and an embryo insertion time of  $5 \times 10^4$  years. The orange and teal lines correspond to the standard and power-law temperature structures. The insert shows the growth of the gaps in the pebble surface density at  $5 \times 10^5$ ,  $7 \times 10^5$ ,  $10^6$ , and  $2 \times 10^6$  years.

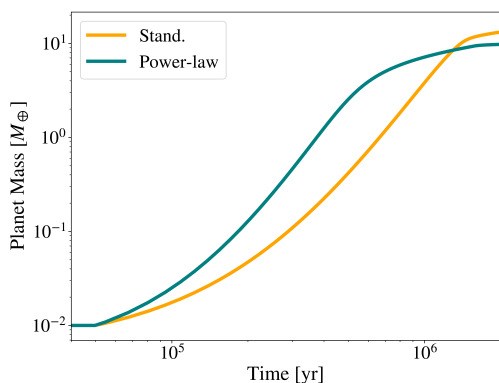


Fig. 9: Growth of a Moon-mass embryo for  $\alpha = 10^{-3}$  from the insertion time until 2 Myr, when the planet growth plateaus. The orange and teal lines show the evolution of the planet mass for the standard and power-law cases.

will be nonzero. In our model, we find that inside 10 AU, planets grow to masses high enough to be the seeds for gas giants. Therefore, the effects of a gaseous envelope will have to be included to model the complete planetary demographics. We have left this for a future study.

#### 4.3. Embryo masses

Recent studies show that the radial location dictates an embryo's initial mass in streaming instability simulations (Liu et al. 2020). As our focus here was the effect that temperature structures have on pebble accretion and planet formation, we chose to keep the initial embryo mass constant, in order to isolate the influence of temperature fluctuations during this study.

#### 4.4. Gap shape

We used the impulse approximation for a planetary torque to form a gap in the gaseous disk by converting it to a gas velocity

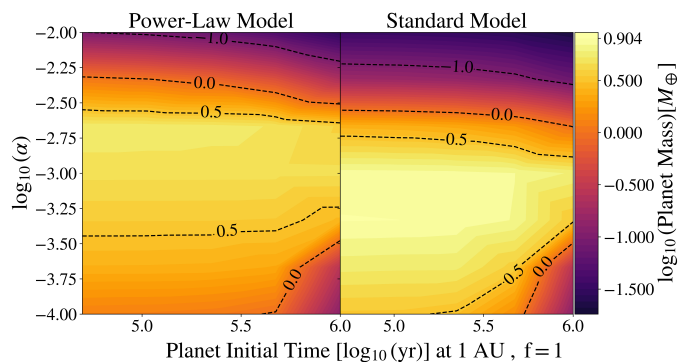


Fig. 10: Same as Fig. 4 but with the torque factor,  $f_\Lambda$ , changed from 0.23 to 1.

(Lin & Papaloizou 1979). This caused a change in the pressure gradient, allowing for pebbles to be slowed and subsequently stopped due to the gap formed by a growing planet. Simulations in 2D and 3D show that gaps formed by 1D approximations overestimate the depth of the gap in the disk. The difference can be as large as two orders of magnitude when compared to similar 2D gap-opening models (Hallam & Paardekooper 2017). To account for this, the impulse approximation used contains a factor  $f_\Lambda$  that is usually taken to be 0.23. We investigated the effect that this factor has on a resulting planetary population. We reran the models at 1 AU using  $f_\Lambda = 1$  (Fig. 10) and compared this to Fig. 4. We find that across all parameters, the final mass of planets formed decreases. The largest planets grown with  $f_\Lambda = 0.23$  are 17 Earth masses, and 8 Earth masses with  $f_\Lambda = 1$ . Modifying this factor shifts the planet population down by a factor of two, meaning it is possible to form more super-Earths and fewer mini-Neptunes. Changing the  $f_\Lambda$  by a factor of five causes the planet to remove material close to its Hill radius, effectively halting the planet-forming process at an earlier stage.

#### 4.5. Migration

Gap formation due to a planet will also lead to planet migration, depending on the planet mass. We omitted planet migration and are aware of the implications. Migrating planets can relocate inward to areas with larger mass budgets and grow into the runaway gas accretion regime. Khorshid et al. (2021) modeled gas giant evolution after the pebble isolation mass is reached and constrained their migration history. They find that, based on a planet's metallicity and C/O ratio, they can predict the initial planet location. These results mirror the importance of migration in another study that finds that the composition of evaporating pebbles can affect the total C/O ratio in gas giant atmospheres (Schneider & Bitsch 2021). This migration process should also affect the pebble composition in intermediate-mass planets, as different radial locations will result in varied bulk compositions. The effect of migration is also left for a future study.

#### 4.6. Comparison to other works

Recent works have also examined the role of pebble accretion and the formation of intermediate-mass planets in the super-Earth and mini-Neptune range (Venturini et al. 2020; Savvidou & Bitsch 2021). Venturini et al. (2020) used a viscous disk, while including photoevaporation in the inner parts of the disk. They also included planet migration and gas accretion, and ignored



1D gap prescriptions. Intriguingly, in the low- $\alpha$  case for our model ( $\alpha = 10^{-4}$ ), we see results similar to theirs for in situ planet formation at 1 AU. They report the largest final mass to be  $2.6M_{\oplus}$ , and we find a mass of  $7M_{\oplus}$ ; there is better agreement when we take the torque factor,  $f_{\Lambda}$ , to be unity, with our highest planet mass being  $3M_{\oplus}$ , as seen in Fig. 10. An increase in  $f_{\Lambda}$  leads to a stronger planetary torque arresting the planet growth at earlier times. The difference in the resulting planet masses shows that our 1D gap prescription overestimates the planet growth by a factor of two when compared to 2D simulations.

Savvidou & Bitsch (2021) explored the formation of super-Earths using 2D simulations in a limited disk region between 0.1 and 4 AU, without gaps, while ignoring planet migration and gas accretion. These models were evolved for a shorter amount of time, until the disk reached thermal equilibrium. Our model has the potential to run for timescales of up to millions of years, allowing us to model the disk evolution over a longer time. Savvidou & Bitsch (2021) took a self-consistent approach to opacities, varying the opacities of various dust species as a function of temperature. They find that the optimal alpha value for the formation of planets large enough to reach the pebble isolation mass is  $\alpha = 10^{-3}$ . Interestingly, with different assumptions and a different modeling setup, we find the same optimal value for alpha. We find that the formulation in our model is sufficient.

## 5. Conclusion

In this work, we developed a semi-analytic model of a protoplanetary disk. We aimed to study the effect that different temperature prescriptions have on the evolution of gas and solids in the disk over time. Knowing the effect of the temperature, we set out to test the effect on a population of pebbles. We find that a power-law prescription initially corresponds to an abundance of pebbles when compared to a dynamic temperature, due to the lack of dust sublimation (Fig. 2). We find that a time-dependent temperature treatment changes the availability and dynamics of pebbles in a significant way. We ran an array of models, varying the disk viscosity, initial embryo formation time, and planetary location. We find that there is a preferred mode for forming larger planets around  $\alpha = 10^{-3}$ , resulting in planets on the order of  $\approx 10M_{\oplus}$ .

To conclude, we find that including viscous heating in an evolving disk leads to changes in the pebble surface density and gap-formation mechanisms. The changes in these two quantities result in planets with higher masses where viscous heating is the primary heating mechanism. Lastly, we find that the inclusion of a dust-sublimation front is beneficial for the growth of super-Earths at a short orbital separation. This could be a possible explanation for the large occurrence of super-Earths at close-in orbits seen in *Kepler* data.

*Acknowledgements.* We thank the anonymous referee for their comments, which greatly improved the manuscript. We acknowledge funding from the European Union H2020-MSCA-ITN-2019 under Grant no. 860470 (CHAMELEON). U.G.J. also acknowledges funding from the Novo Nordisk Foundation Interdisciplinary Synergy Programme grant no. NNF19OC0057374.

## References

Akeson, R. L., Chen, X., Ciardi, D., et al. 2013, *PASP*, 125, 989  
 Alibert, Y., Mordasini, C., Benz, W., & Winisdoerffer, C. 2005, *A&A*, 434, 343  
 Armitage, P. J. 2010, *Astrophysics of Planet Formation*  
 Bean, J. L., Raymond, S. N., & Owen, J. E. 2021, *Journal of Geophysical Research (Planets)*, 126, e06639  
 Birmstiel, T., Andrews, S. M., & Ercolano, B. 2012, *A&A*, 544, A79  
 Birmstiel, T., Dullemond, C. P., & Brauer, F. 2010, *A&A*, 513, A79  
 Bitsch, B. 2019, *A&A*, 630, A51

Bitsch, B., Izidoro, A., Johansen, A., et al. 2019a, *A&A*, 623, A88  
 Bitsch, B., Johansen, A., Lambrechts, M., & Morbidelli, A. 2015, *A&A*, 575, A28  
 Bitsch, B., Morbidelli, A., Johansen, A., et al. 2018, *A&A*, 612, A30  
 Bitsch, B., Raymond, S. N., & Izidoro, A. 2019b, *A&A*, 624, A109  
 Brauer, F., Dullemond, C. P., & Henning, T. 2008, *A&A*, 480, 859  
 Drazkowska, J., Bitsch, B., Lambrechts, M., et al. 2023, *Planet Formation Theory in the Era of ALMA and Kepler: from Pebbles to Exoplanets*  
 Drazkowska, J. & Alibert, Y. 2017, *A&A*, 608, A92  
 Gundlach, B. & Blum, J. 2015, *ApJ*, 798, 34  
 Hallam, P. D. & Paardekooper, S. J. 2017, *MNRAS*, 469, 3813  
 Ida, S., Guillot, T., & Morbidelli, A. 2016, *A&A*, 591, A72  
 Ikoma, M., Nakazawa, K., & Emori, H. 2000, *ApJ*, 537, 1013  
 Johansen, A. & Lambrechts, M. 2017, *Annual Review of Earth and Planetary Sciences*, 45, 359  
 Johansen, A., Mac Low, M.-M., Lacerda, P., & Bizzarro, M. 2015, *Science Advances*, 1, 1500109  
 Johansen, A., Oishi, J. S., Mac Low, M.-M., et al. 2007, *Nature*, 448, 1022  
 Khorshid, N., Min, M., Désert, J. M., Woitke, P., & Dominik, C. 2021, arXiv e-prints, arXiv:2111.00279  
 Kobayashi, H., Kimura, H., Watanabe, S. i., Yamamoto, T., & Müller, S. 2011, *Earth, Planets and Space*, 63, 1067  
 Lambrechts, M. & Johansen, A. 2012, *A&A*, 544, A32  
 Lambrechts, M. & Johansen, A. 2014, *A&A*, 572, A107  
 Lambrechts, M., Johansen, A., & Morbidelli, A. 2014, *A&A*, 572, A35  
 Lambrechts, M., Morbidelli, A., Jacobson, S. A., et al. 2019, *A&A*, 627, A83  
 Li, R. & Youdin, A. N. 2021, *ApJ*, 919, 107  
 Lin, D. & Papaloizou, J. 1979, *MNRAS*, 186, 799  
 Lin, D. N. C. & Papaloizou, J. 1986, *ApJ*, 309, 846  
 Liu, B. & Ji, J. 2020, *Research in Astronomy and Astrophysics*, 20, 164  
 Liu, B., Lambrechts, M., Johansen, A., & Liu, F. 2019, *Astronomy & Astrophysics*, 632, A7  
 Liu, B., Lambrechts, M., Johansen, A., Pascucci, I., & Henning, T. 2020, *A&A*, 638, A88  
 Lynden-Bell, D. & Pringle, J. E. 1974, *MNRAS*, 168, 603  
 Min, M., Dullemond, C. P., Kama, M., & Dominik, C. 2011, *Icarus*, 212, 416  
 Mulders, G. D., Pascucci, I., Apai, D., & Ciesla, F. J. 2018, *AJ*, 156, 24  
 Musiolik, G. & Wurm, G. 2019, *ApJ*, 873, 58  
 Ormel, C. W. 2017, in *Astrophysics and Space Science Library*, Vol. 445, Formation, Evolution, and Dynamics of Young Solar Systems, ed. M. Pessah & O. Gressel, 197  
 Ormel, C. W., Liu, B., & Schoonenberg, D. 2017, *A&A*, 604, A1  
 Pérez, L. M., Chandler, C. J., Isella, A., et al. 2015, *ApJ*, 813, 41  
 Petigura, E. A., Howard, A. W., & Marcy, G. W. 2013, *Proceedings of the National Academy of Science*, 110, 19273  
 Pollack, J. B., Hubickyj, O., Bodenheimer, P., et al. 1996, *Icarus*, 124, 62  
 Savvidou, S. & Bitsch, B. 2021, *A&A*, 650, A132  
 Savvidou, S. & Bitsch, B. 2023, *A&A*, 679, A42  
 Schneider, A. D. & Bitsch, B. 2021, *A&A*, 654, A71  
 Schneider, J., Dedieu, C., Le Sidaner, P., Savalle, R., & Zolotukhin, I. 2011, *A&A*, 532, A79  
 Shakura, N. I. & Sunyaev, R. A. 1973, *A&A*, 24, 337  
 Venturini, J., Guilera, O. M., Ronco, M. P., & Mordasini, C. 2020, *A&A*, 644, A174  
 Weidenschilling, S. J. 1977, *Ap&SS*, 51, 153  
 Whipple, F. L. 1972, in *From Plasma to Planet*, ed. A. Elvius, 211  
 Youdin, A. N. & Goodman, J. 2005, *ApJ*, 620, 459  
 Youdin, A. N. & Lithwick, Y. 2007, *Icarus*, 192, 588  
 Zsom, A., Ormel, C. W., Güttler, C., Blum, J., & Dullemond, C. P. 2010, *A&A*, 513, A57